PHYSICAL REVIEW FLUIDS **4**, 124203 (2019)

Physics of nanoscale immiscible fluid displacement

Gerald J. Wang,[1] Angelo Damone,[2,3] Francesco Benfenati,[3,4] Pietro Poesio,[3]
Gian Paolo Beretta,[3] and Nicolas G. Hadjiconstantinou[1]
[1]*Department of Mechanical Engineering, Massachusetts Institute of Technology, Cambridge, Massachusetts 02139, USA*
[2]*Lehrstuhl für Thermodynamik, Technische Universität Kaiserslautern, Erwin-Schrödinger-Straße 44, Germany*
[3]*Department of Mechanical and Industrial Engineering, Università degli Studi di Brescia, Via Branze 38, 25123 Brescia, Italy*
[4]*Dipartimento di Scienze Fisiche e Chimiche, Universitá degli Studi dell'Aquila, Via Vetoio (Coppito), 67100 L'Aquila, Italy*

(Received 21 March 2019; published 11 December 2019)

We investigate immiscible fluid displacement at small scales where slip lengths are on the order of characteristic system sizes, whereby Cox's law is not expected to be valid. Molecular dynamics simulations show that in this limit hydrodynamic bending becomes small and interfaces remain approximately spherical. In this case the only relevant angle for describing the interface shape is the dynamic *microscopic* angle at the fluid-solid interface. In our simulations, this angle is found to be described well by the molecular-kinetic theory originally proposed by Blake and Haynes. In general, this implies a different functional dependence between the contact angle (and related quantities) and the flow speed (or capillary number); this is demonstrated for the case of the force on the boundary for immiscible fluid displacement in a two-dimensional channel.

DOI: 10.1103/PhysRevFluids.4.124203

I. INTRODUCTION

Immiscible fluid displacement and the motion of contact lines have received enormous attention over the past five decades, both due to the large number of related applications but also due to the rich scientific challenges associated with understanding the dynamics of contact lines and their effect on the fluid motion. These studies have led to a mature understanding of the dynamics of flows involving contact lines and the publication of a number of authoritative reviews on the subject (e.g., see Refs. [1,2]). One crucial conclusion from these studies is that the exact details of the physical mechanism for removing the singularity at the contact line, such as slip, only affect the flow locally and have a small effect on the outer flow [3,4]. In other words, contact-line problems exhibit a convenient scale separation between the internal contact-line dynamics and the external outer flow, thus explaining the universal Tanner-Voinov law [5,6], given in a generalized form by the Cox relation

$$g(\theta_a, \lambda) = g(\theta_e, \lambda) + \mathrm{Ca}\left[\ln(\varepsilon^{-1}) + \frac{Q_1}{f(\theta_e, \lambda)} - \frac{Q_0}{f(\theta_a, \lambda)}\right] + O(\mathrm{Ca}^2), \tag{1}$$

which connects the difference between the apparent (macroscopic) contact angle θ_a—measured at a macroscopic distance d from the contact line—and the equilibrium contact angle θ_e at the fluid-solid boundary to the capillary number, $\mathrm{Ca} = \mu_A U/\gamma$, in the limit $\varepsilon \equiv s/d \to 0$. Here, U is the displacement speed, μ_A is the viscosity of the advancing fluid, γ is the surface tension, and s is the slip length; Q_1 and Q_0 are constants that depend on the details of the flow field in the inner (contact line) and outer regions, respectively. Expressions for the functions $f(\theta, \lambda)$ and $g(\theta, \lambda)$

as a function of the viscosity ratio $\lambda = \mu^B/\mu^A$, where B denotes the receding fluid, are given in Appendix A. In this work, the slip length is defined in the context of the Navier slip boundary condition

$$u_s = s\frac{\partial u}{\partial \eta}\bigg|_w, \tag{2}$$

which relates the slip velocity at the fluid-solid boundary, u_s, to the velocity gradient at the boundary (denoted by subscript w); η denotes the boundary normal pointing into the fluid. Relation (1) assumes that the equilibrium contact angle is equal to the microscopic contact angle at the solid-liquid boundary and that the latter remains fixed for all Ca. This is further discussed in the following sections.

Over the years, the internal contact-line dynamics have been investigated using both theoretical modeling and molecular-dynamics (MD) simulations (see, for example, Refs. [1,7–23]). The primary focus of these studies has been the development of reliable models of the contact-line behavior for use in hydrodynamic descriptions of *macroscopic* problems, that is, systems that exhibit the above-described separation of scales. Although deviations from the macroscopic behavior due to the presence of nanoscale phenomena have been studied on some occasions in their own right (e.g., see Refs. [24,25]), a comprehensive understanding of the dynamics of capillary flow of immiscible fluids under nanoscale conditions has yet to be completed.

In this paper, motivated by recent interest in nanoscale flows, we use MD simulations to study *nanoscale* immiscible displacement flows for which the traditional description based on the Tanner-Voinov law is not expected to hold. Specifically, we study the flow of water and pentane in two-dimensional capillaries of height $H = 30$–40 Å. Even though the Navier-Stokes description remains valid at these scales (e.g., see Ref. [26] for discussion), we expect deviations from the Tanner-Voinov law since the above-described separation of scales does not necessarily exist. Particularly important is the presence of slip in these flows [27], which is not compatible with relation (1), since the latter relies on the presence of no-slip conditions at distances $d \gg s$ away from the contact line [3]. In other words, we study immiscible displacement under conditions $s \sim H$ ($\sim d$) seeking to develop an understanding towards a description that replaces relation (1).

II. MOLECULAR-DYNAMICS SIMULATIONS

To investigate capillary flow in the regime where the slip length is on the order of the characteristic flow length scale, we performed MD simulations of water displacing pentane in a two-dimensional nano-slit of length $L = L_1 + L_2 = 160$ Å and height $H = 2h$ in the low-Ca limit (see Fig. 1) at a temperature of $T = 300$ K. Each simulation was run for 10 ns, utilizing

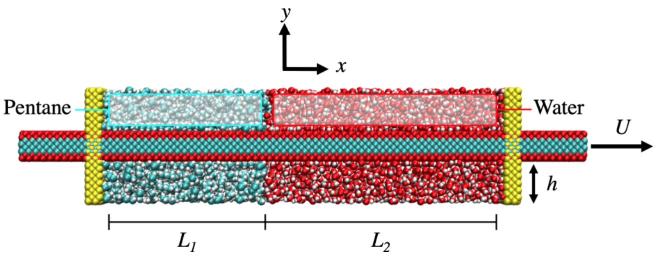

FIG. 1. MD System Setup: The solid wall serves to bound the fluids in a slit geometry; it also imposes a translation speed of U in the positive x direction. The wall consists of two different groups of wall particles (interactions are identical), shown in cyan and red. The former (inner) group is not thermostatted and is used to impose the translation of the whole structure; the latter (outer) group, is thermostatted using a Langevin thermostat. Fixed walls that constrain the fluid in the axial direction are shown in yellow. Periodic boundary conditions are imposed in all dimensions.

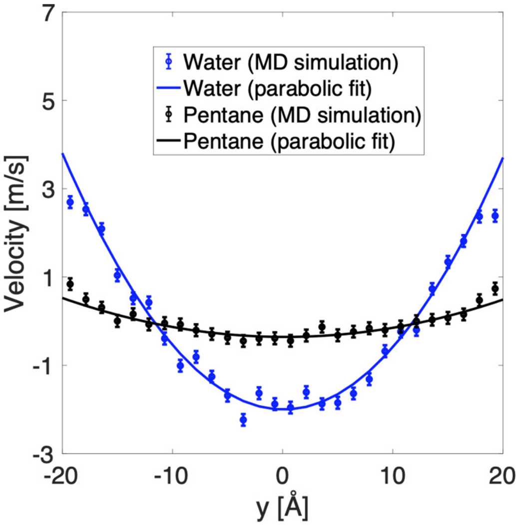

FIG. 2. Water (blue) and pentane (black) velocity profiles as a function of the transverse dimension, obtained from MD simulation, with parabolic fits overlaid. Note that these coordinates are shifted such that $y = \pm 20$ Å corresponds to the locations of the walls and $y = 0$ Å corresponds to the location at which the periodic boundary condition is applied.

a time step of 1 fs. By applying periodic boundary conditions in the transverse (y) direction, the fluids can be confined laterally using a single solid wall translating with velocity U in the positive x direction. Particles within this wall interact via a Lennard-Jones potential [28] with length scale $\sigma_w = 1.7025$ Å, energy scale $\varepsilon_w = 1.08$ eV, and cutoff radius $r_c = 2.5\sigma_w$. Periodic boundary conditions are also applied in the depth (z) direction, in which the simulation is homogeneous. We note that here, H denotes the extent of the domain occupied by fluid; the distance between the walls (two sides of the same wall across the fluid, in the present implementation) is approximately two molecular diameters larger due to the standoff distance between the fluid and the solid, which is nonnegligible at the scales considered here [29–31]. The fluids are confined in the axial (x) direction by additional impermeable walls held at a fixed temperature using a Nosé-Hoover thermostat. These walls interact only with fluid molecules.

The interaction between the solid and the liquid molecules is modeled with a modified Lennard-Jones potential:

$$U_{\mathrm{LJ}}(r_{ij}) = 4\varepsilon_{\mathrm{wf}}\left[\left(\frac{\sigma_{\mathrm{wf}}}{r_{ij}}\right)^{12} - \beta_{ij}\left(\frac{\sigma_{\mathrm{wf}}}{r_{ij}}\right)^{6}\right], \tag{3}$$

where $\sigma_{\mathrm{wf}} = 1.4$ Å and a cutoff radius of $r_c = 10$ Å. The coefficient β_{ij} takes on different values for the two liquids to tune their relative wettabilities. In this work, we have taken $\beta_{ij}^w = 0.26$ for water-solid interactions and $\beta_{ij}^p = 0.17$ or 0.21 for pentane-solid interactions. Three different values of the interaction strength $\varepsilon_{\mathrm{wf}}$ were simulated, namely, $\varepsilon_{\mathrm{wf}} = 0.06$, 0.09, and 0.18 eV.

Pentane was modeled using the standard Optimized Potential for Liquid Simulation (OPLS-AA) [32], while water was modeled with the TIP4P/2005 potential [33]. Lorentz-Berthelot combination rules give the interaction between water and pentane.

Figure 2 shows the water and pentane velocity profiles as a function of the transverse dimension, for the case $U = 7$ m/s, $H = 40$ Å, $\varepsilon_{\mathrm{wf}} = 0.18$ eV, and $\beta_{ij}^p = 0.21$, averaged over the region $20\,\text{Å} < |x - x_0| < 60$ Å for each fluid, respectively, where x_0 is the average position of the water-pentane interface. For $U > 0$ water is the advancing fluid. The averaging region was chosen to be sufficiently far from the interface region ($|x - x_0| \lesssim 10$ Å) for fully developed conditions to be valid (and thus Poiseuille profiles to appear if the Navier-Stokes description is valid). Statistical uncertainty was estimated using the formulation described in Ref. [34]; statistical inefficiency (sample decorrelation time) was estimated based on the formulation described in Ref. [28] yielding a decorrelation time of 1 ns. Figure 2 shows that parabolic profiles are indeed excellent approximations to the MD data, albeit with substantial slip; this is in general agreement with previous work [26]. Specifically, using the Navier condition (2) with $s = \alpha h$, we find $\alpha_w = 0.33$ for water and $\alpha_p = 2.5$ for pentane. These slip values, namely $\alpha_w h \sim 0.6$ nm and $\alpha_p h \sim 5$ nm, are generally consistent with typical values reported in the literature based on MD simulations and experiments [35,36].

The relatively low flow velocities used here are computationally expensive to discern accurately in the presence of molecular fluctuations; in particular, the computational cost for resolving a particular flow velocity magnitude to a given relative statistical uncertainty increases quadratically with the inverse of the Mach number, in the small-Mach-number limit [34]. For this reason, we did not attempt to measure the slip length of any of the other sets of interactions; these slip lengths are expected [37] to be larger given the weaker fluid-solid interactions in these simulations, which lead to even smaller flow velocities.

III. MOLECULAR-DYNAMICS SIMULATION RESULTS

In this section we present and discuss our MD simulation results. The majority of these results were obtained using $\beta_{ij}^{p} = 0.21$; this value yields contact angles in the range $70^\circ \lesssim \theta \lesssim 110^\circ$ ($|\cos(\theta)| \lesssim 0.4$), for which circular interfaces can be approximated as parabolic. As explained below, this simplifies the analysis considerably. Simulations for $\beta_{ij}^{p} = 0.17$, which results in a fully wetting system and in dynamic contact angles in the range $15^\circ \lesssim \theta \lesssim 100^\circ$, have also been performed; they are discussed in Sec. III B. The interface shape fits discussed in Secs. III A and III B exclude data in a region of width $1.5\sigma_{\text{wf}}$ from each wall to avoid the oscillatory statistics resulting from fluid layering that is well known to occur near fluid-solid interfaces [29,31].

A. Dynamic contact angle as a function of Ca

In this section we discuss the contact angle and interface shape behavior obtained using $\beta_{ij}^{p} = 0.21$. We extract the interface shape using least-squares parabolic fits (and excluding data $1.5\sigma_{\text{wf}}$ from each wall). Parabolic fits were preferred as we found them to be less sensitive to layering than circular fits (although very diminished, fluid layering persists for a few molecular length scales beyond $1.5\sigma_{\text{wf}}$ from the walls). As can be seen in the example of Fig. 3, these parabolic fits match the interface shapes very well ($R^2 > 0.9$ for all cases, usually $R^2 > 0.95$). Given that for the shapes considered here a parabola is a good approximation to a circular segment, we conclude that the interface shape remains circular (spherical in 3D), as expected.

The contact angle θ is defined as the angle between the tangent to the interface and the unit vector in the x direction, as shown in Fig. 3. This angle is calculated from the slope (evaluated at the two ends of the fluid region, $y = \pm 20$ Å, and subsequently averaged) of the fit to the interface shape. The uncertainty in $\cos(\theta)$ shown in the figures is propagated from our uncertainty in θ estimated to be $\pm 2^\circ$; for this purpose, for the values of θ encountered in this section ($70^\circ \lesssim \theta \lesssim 110^\circ$) we have taken $\sin(\theta) \approx 1$.

The circular interface shapes found here suggest that, contrary to macroscopic flows, no "hydrodynamic bending" is evident close to the contact line; the term "hydrodynamic" is used here to include the general case where length scales are sufficiently small that the Navier-Stokes description is no longer valid (and thus shear stresses may, technically, not be viscous). The lack of hydrodynamic bending in MD simulations has been observed and remarked upon before [16,19], although no detailed explanation for this behavior was pursued. From the macroscopic point of view, this behavior should not be very surprising: it can be seen clearly from the Cox relation that the interface deflection [as measured by $g(\theta_a) - g(\theta_e)$] decreases monotonically with increasing

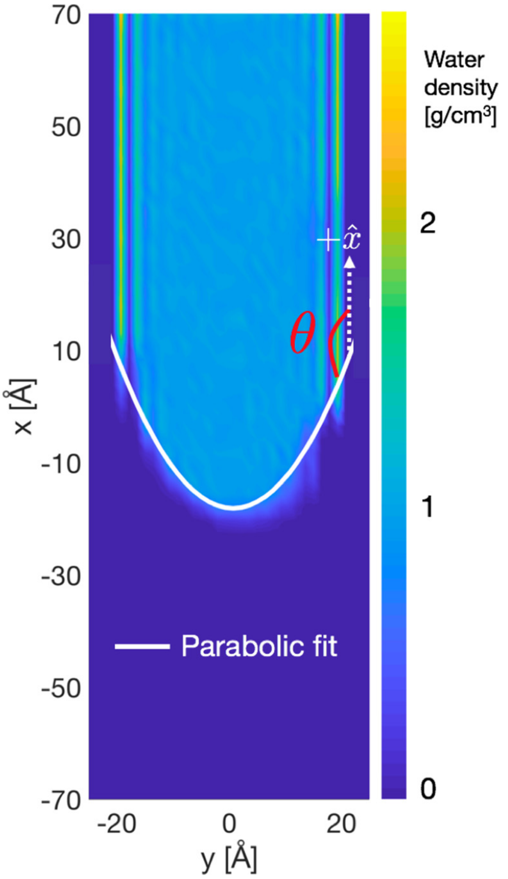

FIG. 3. Density profile for water obtained from MD simulation along with a parabolic fit ($R^2 = 0.96$) to the fluid-fluid interface. The positive axial (x) direction is shown by the dashed arrow; the contact angle θ (measured in the water phase) is shown in red. This simulation was performed at Ca $= 0.04$ and $\varepsilon_{\mathrm{wf}} = 0.12$ eV, with $U > 0$ in the $+\hat{x}$ direction.

$s \sim \alpha h$. Since the Cox relation is not expected to hold as $\alpha \to 1$, we have performed finite element simulations of this scenario which verify that $g(\theta_a) - g(\theta_e)$ continues to decrease as α increases and becomes of order 1. These simulations are discussed in Appendix B.

The absence of hydrodynamic bending close to the contact line is of course a manifestation of the fact that as s becomes on the order of d, a distinct inner and outer region can no longer be defined. As a consequence of the above observation, an apparent contact angle that quantifies the difference between the microscopic dynamic contact angle at the fluid-solid boundary and the dynamic contact angle observed macroscopically is no longer needed. In other words, for the nanoscale problems studied here, the microscopic dynamic contact angle (at the fluid-solid boundary), θ, becomes the only relevant angle. Figure 4 shows its dependence on Ca for three different fluid-wall interaction strengths explored in this study. This data can be fitted well using the expression

$$\cos(\theta) = \cos(\theta_e) - \frac{2k_BT}{\gamma \ell_j^2}\sinh^{-1}\left(\frac{\gamma\tau_0 e^{V/k_BT}}{2\mu_A \ell_j}\mathrm{Ca}\right), \tag{4}$$

obtained from Blake and Hayne's molecular-kinetic theory (MKT) [2,7] on identifying the driving force for the contact-line motion as the uncompensated Young force $\gamma[\cos(\theta) - \cos(\theta_e)]$. Here, ℓ_j is the molecular jump distance for liquid molecules along the solid, τ_0^{-1} is the jump-attempt

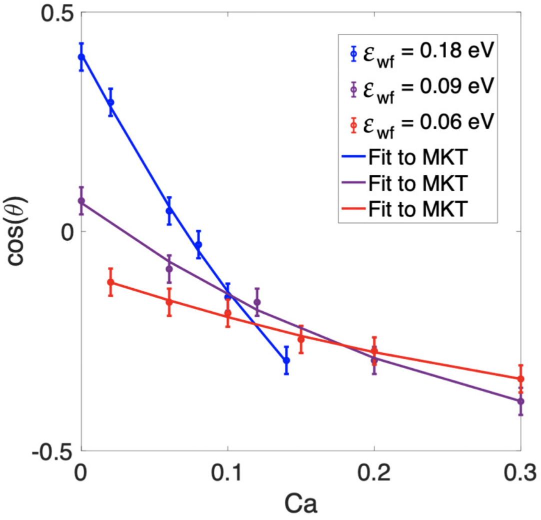

FIG. 4. Dynamic contact angles as a function of Ca, for various wall-fluid interactions for $H = 40$ Å. Solid lines denote fits to MD data (symbols) using Eq. (4).

frequency, V is the potential barrier height associated with the jump process, and k_B is Boltzmann's constant. This theory has been the subject of an extensive investigation by Blake, De Coninck, and collaborators (see, for example, Refs. [14–16,18,19,21]), as well as others [22,23] spanning more than two decades and involving comparisons between analytical models, MD simulations, and experiments. Taken as a whole, this body of previous work provides very strong evidence that, when driving forces are small enough, the linearized version of the molecular-kinetic theory can capture the dissipation associated with contact-line motion to a very good extent.

As can be visually verified from Fig. 4, our simulations correspond to the (weakly) nonlinear regime that has been significantly harder to access. The figure also shows two-parameter fits of the form $\cos(\theta) = \cos(\theta_e) + c_1 \sinh^{-1}(c_2\text{Ca})$ to the MD data. The resulting fit values for coefficient c_2 range from $\sim$5 ($\varepsilon_{\text{wf}} = 0.06$) to $\sim$10 ($\varepsilon_{\text{wf}} = 0.18$), verifying that our data indeed lies in the nonlinear regime. Repeating these fits using the linearized form of Eq. (4) leads to residual norms that are larger by a factor of 2 to 10.

Using the values of parameters c_1 and c_2, as well as $\mu_A = 10^{-3}$ Pa s and $\gamma = 0.05$ N/m [38], we find $\ell_j \sim O(7$ Å$)$ and $\tau_0 \exp(V/k_BT) \sim O(0.2\,\text{ns})$ (see Table I for precise values). Here we note that a process for accurately determining the molecular parameters featuring in Eq. (4) from MD simulations has already been developed and refined [16,20]. However, the present much simpler approach suffices since our objective here is to ensure that the fits shown in the figure are physically meaningful, by verifying that the fit parameters are of the right magnitude. As Table I shows, the resulting values are indeed of the correct magnitude and in good qualitative agreement with the

TABLE I. Parameters for molecular-kinetic theory in Eq. (4), as a function of fluid-solid interaction strength. The 95% confidence intervals for ℓ_j and $\tau_0 \exp(V/k_BT)$ are ±0.3 Å and ±0.02 ns, respectively.

ε_{wf} [eV]	ℓ_j [Å]	$\tau_0 \exp(V/k_BT)$ [ns]
0.06	9.5	0.21
0.09	7.9	0.27
0.18	5.1	0.20

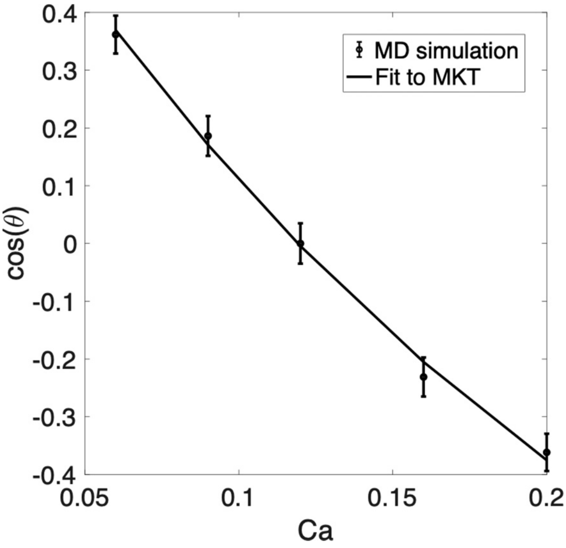

FIG. 5. Dynamic contact angles as a function of Ca, for $\varepsilon_{\mathrm{wf}} = 0.18$ eV, $\beta_{ij}^{p} = 0.21$, and $H = 30$ Å. The solid line denotes a fit to MD data (symbols) using Eq. (4).

results of Bertrand *et al.* [20] and Ren *et al.* [13]; of particular note is the agreement with the observation of Ren *et al.* that the characteristic length scale associated with the molecular jump distance is slightly larger than the spacing of atomic sites in the solid. We find this behavior to be consistent with our physical picture of the molecular-kinetic theory [37]: The potential barrier associated with fluid motion at the fluid-solid interface involves contributions from both the fluid-solid interaction and the fluid-fluid interaction (from the fluid layers adjacent to the interfacial); as the fluid-solid interaction becomes stronger, it tends to dominate, causing the jump length to approach the interatomic spacing in the solid.

Figure 5 shows the dependence of θ on Ca for the strongest wall-fluid interaction ($\varepsilon_{\mathrm{wf}} = 0.18$ eV) in a narrower channel ($H = 30$ Å); the agreement between the MD data and Eq. (4) remains very good.

B. Wetting case

To ensure that our MD results indeed support Eq. (4) over a wider range of contact angles, including in regimes where it does not linearize to a relation of the form $\theta - \theta_e \propto \mathrm{Ca}$ (similar to the Cox relation, at least in linearized form), we performed simulations for the case $\varepsilon_{\mathrm{wf}} = 0.18$ eV using $\beta_{ij}^{p} = 0.17$ for a channel height $H = 40$ Å. This choice yields a very small value of equilibrium contact angle ($\theta_e \approx 0^\circ$ for $U = 0$) and thus allows for testing the validity of Eq. (4) in a regime where it linearizes to $\theta^2 - \theta_e^2 \sim \mathrm{Ca}$. Moreover, the smaller equilibrium contact angle means that larger values of Ca can be reached before the interface breaks, allowing us to probe the validity of Eq. (4) over a greater range of capillary number values.

In this more general case, interface shapes were fitted using circular fits, since the condition $|\cos(\theta)| \lesssim 0.4$ no longer holds for all measurements. The contact angle was measured as the average of the slopes of a circular fit at $y = \pm 19$ Å. The results for the dynamic contact angle are shown in Fig. 6. The fit to these results, also shown in the figure, suggests that Eq. (4) is capable of describing this data accurately.

C. Frictional force on the solid boundary

A direct consequence of the behavior described above is that the frictional force on the wall has a different dependence on Ca compared to the case where the apparent contact angle obeys the Cox

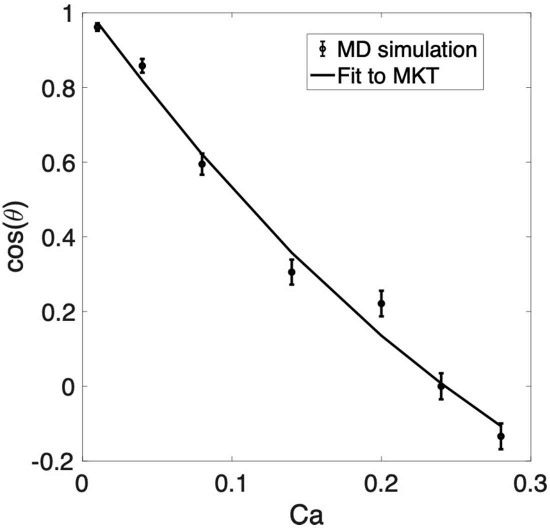

FIG. 6. Dynamic contact angles as a function of Ca, for $\varepsilon_{\rm wf} = 0.18$ eV, $\beta_{ij}^{p} = 0.17$, and $H = 40$ Å. The solid line denotes fit to MD data (symbols) using Eq. (4).

relation, Eq. (1). Let us write

$$F_w = F_{\rm CL} + (\tau_s)_p L_1 + (\tau_s)_w L_2 \tag{5}$$

to describe the magnitude of the force per unit contact-line length acting on one of the solid boundaries. In this relation, $(\tau_s)_p$ and $(\tau_s)_w$ denote the magnitudes of the shear stress at the wall in the pentane and water regions respectively, while $F_{\rm CL}$ denotes the magnitude of the total force (per unit contact-line length) resisting the contact-line motion. To connect $F_{\rm CL}$ to the microscopic dynamic contact angle, we use the relation

$$F_{\rm CL} = \gamma[\cos(\theta_e) - \cos(\theta)] + \chi U, \tag{6}$$

obtained by Ren and E [13] by performing a force balance on a control volume including the contact line and extending ±10 Å from the contact line in the x direction and 8 Å from the wall and into the fluid in the y direction. In other words, $F_{\rm CL}$ is the total force felt by the contact-line region summed over a finite (but molecularly small) distance ($\sim$20 Å); the finite size of this distance was neglected in writing Eq. (5). According to Eq. (6), $F_{\rm CL}$ includes contributions both from the imbalance of surface tension forces at the contact line and the normal stress jump at the two-fluid interface. The latter was shown by Ren and E to be proportional to the contact-line velocity in the linear regime. Since its origin is in the hydrodynamic stress associated with the flow velocity, we assume that it continues to be given by the form χU even in the regime where the nonlinearity is important [as manifested, for example, in the nonlinear relation between θ and U in Eq. (4)]; here χ denotes a proportionality constant with units of viscosity.

By virtue of Eq. (4), $F_{\rm CL}$ is thus expected to be of the form

$$F_{\rm CL} = c_0 {\rm Ca} + c_1 \gamma \sinh^{-1}(c_2 {\rm Ca}). \tag{7}$$

To verify this, we measured the total force on the boundary in simulations with parameters $H =$ 40 Å, $\varepsilon_{\rm wf} = 0.18$ eV, and $\beta_{ij}^{p} = 0.21$. The top panel of Fig. 7 shows MD simulation results for this direct measurement of F_w as a function of Ca. Statistical uncertainty was estimated using the sample variance corrected for statistical inefficiency using the technique described in Ref. [28]. The figure also shows a fit to the simulation data, from which we extract values for the coefficients c_0, c_1, and c_2 defined in Eq. (7). For this fit, the Poiseuille contribution of the wall shear stress was assumed

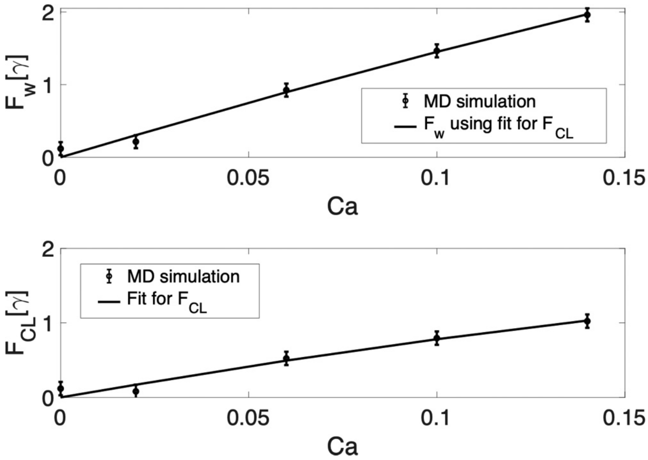

FIG. 7. Magnitude of force per unit contact-line length on the solid boundary (top) and in the contact-line region (bottom) as a function of Ca, for $\varepsilon_{\mathrm{wf}} = 0.18$ eV, $\beta_{ij}^p = 0.21$, and $H = 40$ Å. Solid lines denote fits to MD data (symbols) as explained in the text. Forces per unit length are normalized by surface tension γ.

known and equal to $(\tau_s)_j = 3\mu_j U/[h(1 + 3\alpha_j)]$ for $j \in \{p, w\}$. Taking $\gamma = 0.05$ N/m (as before), the resulting fit gives estimates of $c_1 = 0.68$ and $c_2 = 9.7$, which are in excellent agreement with the values obtained in Sec. III A (where the corresponding prefactor and exponent of the $\sinh^{-1}$ function were $c_1 = 0.64$ and $c_2 = 9.5$). The bottom panel of the same figure shows the magnitude of the force on the contact line, F_{CL}, obtained by subtracting the viscous contribution (calculated from the viscous model explained above) from F_w, per Eq. (5). The solid line shows the fit to Eq. (7) obtained as described above.

Here we note that the force measurement on the solid boundary is independent of the direct angle measurements shown in Figs. 4–6 that led to the original adoption of Eq. (4) for describing the dynamic contact angle. The excellent agreement shown in Fig. 7 therefore serves as an independent validation, making the close agreement between the fitting constants particularly gratifying.

IV. DISCUSSION AND CONCLUSIONS

Molecular dynamics and continuum simulations (finite element solution of the Stokes set) of immiscible fluid displacement show that at the nanoscale, when slip lengths become appreciable as a function of the flow characteristic length scale, hydrodynamic deformation of the interface becomes small. As a result, interface shapes remain to a good approximation spherical throughout the physical domain (at least for Ca $\lesssim 0.2$) and the distinction between the apparent and microscopic dynamic angles disappears. In other words, the dynamic interface shape becomes an extension of the static case, with the microscopic contact angle, in general a function of the capillary number, determining the interface (constant) curvature by setting the contact angle at the boundary. Direct measurement of this contact angle in MD simulations shows that this angle is determined by molecular-kinetic considerations; specifically, good agreement is found between our results and the nonlinear form of the molecular-kinetic model of Blake and Haynes [7] in which the contact-line motion is modeled as a thermally activated process with the uncompensated Young force acting as the driving force. As expected from such a model, the contact-angle response to shear is very sensitive to the fluid-solid interaction strength. Decreasing this interaction strength results in appreciable decrease in the interface deflection (with respect to the equilibrium configuration) in the presence of flow.

The above conclusions are consistent with the findings of the very careful studies by Ruijter *et al.* [16] (see also the discussion in Ref. [19] and references therein) and Heine *et al.* [22,23] who, in the process of validating the (linear version of the) molecular-kinetic theory, compared MD simulations of droplet spreading to a simple analytical model of the same. Assuming that the droplet remained spherical in shape, this analytical model combined an approximate representation of the flow inside the droplet with the linearized molecular-kinetic theory for the contact-line behavior [linear form of Eq. (4)] to yield the spreading velocity as a function of time. Both groups showed that their MD simulation results could be explained by neglecting the hydrodynamic component of the model, that is, the contribution of viscous dissipation was small. Although this was attributed to the particular parameters of the simulation (e.g., large equilibrium contact angle and small viscosity in Ref. [16]), our results and discussion provide the further insight that a significant and general contributor to the diminished importance of viscous dissipation is the presence of slip which eventually becomes important as length scales decrease, but was neglected in the simple analytical model.

The frictional force opposing the contact-line motion was found to be in good agreement with the relation developed by Ren and E [13]. As we show in Sec. III C, this relation and knowledge of the contact-angle dependence on the capillary number via Eq. (4) allows us to express the frictional force as an explicit function of the capillary number.

Although hydrodynamic bending was negligible in our simulations, it is expected that in other situations such as, for example, systems at length scales larger than the ones considered here, the contact angle will be influenced by both molecular-kinetic effects (to the extent those are present) and hydrodynamic bending. In fact the relative importance of the two types of dissipation will, in general, depend on the particular problem of interest (see Heine *et al.* [22,23] for an example where the problem dimensionality alters the balance between molecular and macroscopic effects). In cases where the hydrodynamic bending effects are consistent with Cox's law, the two contributions can be combined as previously described in Ref. [39] (see also discussion in Sec. III D 2 in Ref. [2]). However, when length scales are sufficiently small that hydrodynamic bending is not described by Cox's law, a combined description is currently not available [18,19]. Future work will focus on this regime, perhaps by first developing a general criterion for estimating the relative contribution of hydrodynamic bending and molecular-kinetic effects.

ACKNOWLEDGMENTS

This work was supported, in part, by Aramco Services Company. The authors thank Drs. Vinay Raman and Michael Szulczewski for many stimulating discussions. G.J.W. was supported by the DOE CSGF (Contract No. DE-FG02-97ER25308).

APPENDIX A: THE COX RELATION FOR THE APPARENT CONTACT ANGLE

The $g(\theta)$ function appearing in the Cox relation, Eq. (1), is given by

$$g(\theta) = \int_0^\theta \frac{d\theta'}{f(\theta')}, \tag{A1}$$

where

$$f(\theta) = \frac{2\{\lambda^2(\theta^2 - \sin^2\theta) + 2\lambda[\theta(\pi - \theta) + \sin^2\theta] + [(\pi - \theta)^2 - \sin^2\theta]\}\sin\theta}{\lambda(\theta^2 - \sin^2\theta)[(\pi - \theta) + \sin\theta\cos\theta] + [(\pi - \theta)^2 - \sin^2\theta](\theta - \sin\theta\cos\theta)}. \tag{A2}$$

APPENDIX B: APPARENT CONTACT ANGLE IN THE PRESENCE OF SIGNIFICANT SLIP ACCORDING TO CONTINUUM THEORY

In this Appendix we examine, from a continuum point of view, the limit in which the slip length s is not negligible compared to the outer flow characteristic length scale h. In general, as slip increases, we expect that the degree of viscous bending will decrease. This is consistent with the Cox relation, which predicts a logarithmic decrease in $g(\theta_a) - g(\theta_e)$ as $\varepsilon = s/d$ increases (provided it remains

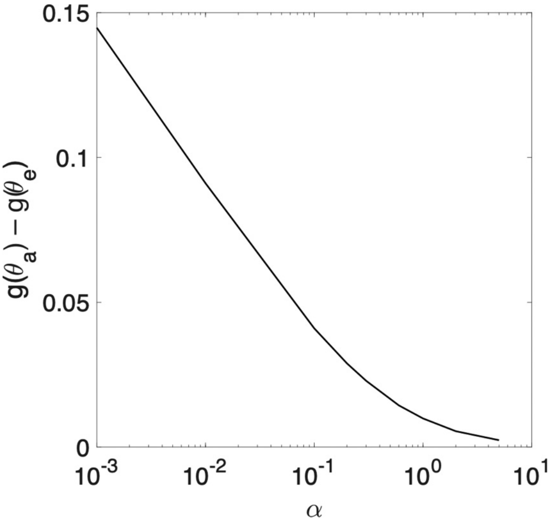

FIG. 8. Degree of bending, as measured by $g(\theta_a) - g(\theta_e)$ as a function of the nondimensional slip length, α for $\lambda = 1$. The logarithmic dependence of $g(\theta_a) - g(\theta_e)$ on α for $\alpha \ll 1$ is clearly visible.

small). As ε increases further, such that the term $\mathrm{Ca}\ln(\varepsilon^{-1})$ is no longer dominant compared to the terms containing Q_1 and Q_0, the dependence is no longer logarithmic. If ε increases further still, then the Cox relation is expected to no longer be accurate, as it is an asymptotic result valid in the limit $\varepsilon \to 0$.

To investigate the dependence of viscous bending on the slip length in the limit $\varepsilon \sim O(1)$, we performed finite element simulations of immiscible displacement in the geometry of Fig. 1 using the method described in Ref. [40]. Figure 8 shows the difference $g(\theta_a) - g(\theta_e)$ as a function of $\alpha = s/h$ for the case $\mathrm{Ca} = 0.025$, $\theta_e = \pi/2$, and $\lambda = 1$; θ_a was measured using the definition [4]

$$\theta_a = \tan^{-1}\left[\frac{1-\ell^2}{2\ell}\right], \tag{B1}$$

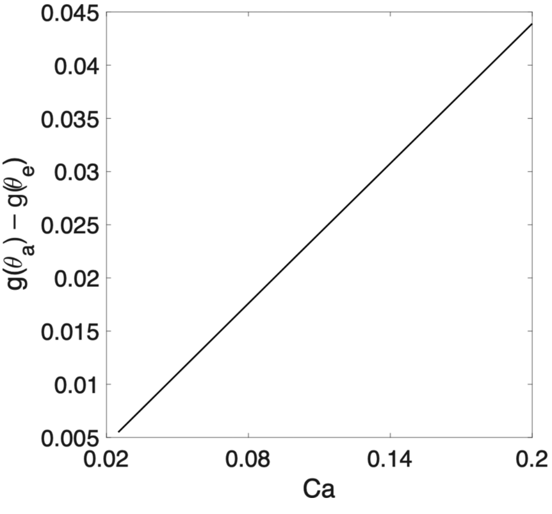

FIG. 9. Degree of bending, as measured by $g(\theta_a) - g(\theta_e)$ as a function of Ca, for $\alpha = 2$, $\theta_e = \pi/2$ and $\lambda = 1$.

where ℓ denotes the "rise" of the interface curve (measured from the contact-line plane). The figure verifies the logarithmic dependence of $g(\theta_a) - g(\theta_e)$ on α when $\alpha \sim \varepsilon \ll 1$ and shows that, as α increases to be of order one, $\theta_a - \theta_e \propto g(\theta_a) - g(\theta_e)$ continues to decrease monotonically, albeit no longer logarithmically.

To provide as close a comparison as possible to our MD results discussed in Sec. III, we performed finite element simulations at $\lambda = 1$, $\theta_e = \pi/2$ and $\alpha = 2$ for various values of Ca; the results for the dynamic contact angle response, shown in Fig. 9, can be summarized by the approximate (empirical) relation $\theta_a - \theta_e \approx \mathrm{Ca}$ for $0 \leqslant \mathrm{Ca} \lesssim 0.2$. These deformations are negligible compared to the angle variations observed in our simulations (see, for example, Fig. 6), leading us to conclude that the changes in the contact angle observed in the MD simulations are due to a different mechanism than the hydrodynamic bending described by the Cox relation.

[1] P. G. de Gennes, Wetting: Statics and dynamics, Rev. Mod. Phys. **57**, 827 (1985).
[2] D. Bonn, J. Eggers, J. Indekeu, J. Meunier, and E. Rolley, Wetting and spreading, Rev. Mod. Phys. **81**, 739 (2009).
[3] R. G. Cox, The dynamics of the spreading of liquids on a solid surface. Part 1. Viscous flow, J. Fluid Mech. **168**, 169 (1986).
[4] P. Sheng and M. Zhou, Immiscible-fluid displacement: Contact-line dynamics and the velocity-dependent capillary pressure, Phys. Rev. A **45**, 5694 (1992).
[5] O. V. Voinov, Hydrodynamics of wetting, Fluid Dyn. **11**, 714 (1976).
[6] L. H. Tanner, The spreading of silicone oil drops on horizontal surfaces, J. Phys. D **12**, 1473 (1979).
[7] T. D. Blake and J. M Haynes, Kinetics of liquid/liquid displacement, J. Colloid Interface Sci. **30**, 421 (1969).
[8] P. A. Thompson and M. O. Robbins, Simulations of Contact-Line Motion: Slip and the Dynamic Contact Angle, Phys. Rev. Lett. **63**, 766 (1989).
[9] N. G. Hadjiconstantinou, Combining atomistic and continuum simulations of contact-line motion, Phys. Rev. E **59**, 2475 (1999).
[10] G. He and N. G. Hadjiconstantinou, A molecular view of Tanner's law: Molecular dynamics simulations of droplet spreading, J. Fluid Mech. **497**, 123 (2003).
[11] T. Qian, X.-P. Wang, and P. Sheng, Molecular scale contact-line hydrodynamics of immiscible flows, Phys. Rev. E **68**, 016306 (2003).
[12] T. Qian, X.-P. Wang, and P. Sheng, Power-Law Slip Profile of the Moving Contact Line in Two-Phase Immiscible Flows, Phys. Rev. Lett. **93**, 094501 (2004).
[13] W. Ren and W. E, Boundary conditions for the moving contact-line problem, Phys. Fluids **19**, 022101 (2007).
[14] T. D. Blake, A. Clarke, J. De Coninck, and M. J. de Ruijter, Contact angle relaxation during droplet spreading: Comparison between molecular kinetic theory and molecular dynamics, Langmuir **13**, 2164 (1997).
[15] M. J. de Ruijter, J. De Coninck, T. D. Blake, A. Clarke, and A. Rankin, Contact angle relaxation during the spreading of partially wetting drops, Langmuir **13**, 7293 (1997).
[16] M. J. de Ruijter, T. D. Blake, and J. De Coninck, Dynamic wetting studied by molecular modeling simulations of droplet spreading, Langmuir **15**, 7836 (1999).
[17] T. D. Blake and J. De Coninck, The influence of solid-liquid interactions on dynamic wetting, Adv. Colloid Interface Sci. **96**, 21 (2002), a Collection of Papers in Honour of Nikolay Churaev on the Occasion of his 80th Birthday.
[18] G. Martic, F. Gentner, D. Seveno, J. De Coninck, and T. D. Blake, The possibility of different time scales in the dynamics of pore imbibition, J. Colloid Interface Sci. **270**, 171 (2004).
[19] T. D. Blake, The physics of moving wetting lines, J. Colloid Interface Sci. **299**, 1 (2006).

[20] E. Bertrand, T. D. Blake, and J. De Coninck, Influence of solid–liquid interactions on dynamic wetting: A molecular dynamics study, J. Phys. Condens. Matter **21**, 464124 (2009).

[21] J.-C. Fernández-Toledano, T. D. Blake, and J. De Coninck, Contact-line fluctuations and dynamic wetting, J. Colloid Interface Sci. **540**, 322 (2019).

[22] D. R. Heine, G. S. Grest, and E. B. Webb, Spreading dynamics of polymer nanodroplets, Phys. Rev. E **68**, 061603 (2003).

[23] D. R. Heine, G. S. Grest, and E. B. Webb, Spreading dynamics of polymer nanodroplets in cylindrical geometries, Phys. Rev. E **70**, 011606 (2004).

[24] S. Gravelle, C. Ybert, L. Bocquet, and L. Joly, Anomalous capillary filling and wettability reversal in nanochannels, Phys. Rev. E **93**, 033123 (2016).

[25] Y. Qiao, L. Liu, and X. Chen, Pressurized liquid in nanopores: A modified Laplace-Young equation, Nano Lett. **9**, 984 (2009).

[26] N. Chandramoorthy and N. G. Hadjiconstantinou, Solving lubrication problems at the nanometer scale, Microfluid. Nanofluid. **22**, 48 (2018).

[27] L. Bocquet and J.-L. Barrat, Flow boundary conditions from nano- to micro-scales, Soft Matter **3**, 685 (2007).

[28] M. P. Allen and D. J. Tildesley, *Computer Simulation of Liquids* (Oxford University Press, Oxford, 1989).

[29] L. A. Rowley, D. Nicholson, and N. G. Parsonage, Grand ensemble Monte Carlo studies of physical adsorption, Mol. Phys. **31**, 389 (1976).

[30] G. J. Wang and N. G. Hadjiconstantinou, Why are fluid densities so low in carbon nanotubes? Phys. Fluids **27**, 052006 (2015).

[31] G. J. Wang and N. G. Hadjiconstantinou, Molecular mechanics and structure of the fluid-solid interface in simple fluids, Phys. Rev. Fluids **2**, 094201 (2017).

[32] W. L. Jorgensen, D. S. Maxwell, and J. Tirado-Rives, Development and testing of the OPLS all-atom force field on conformational energetics and properties of organic liquids, J. Am. Chem. Soc. **118**, 11225 (1996).

[33] J. L. F. Abascal and C. Vega, A general purpose model for the condensed phases of water: Tip4p/2005, J. Chem. Phys. **123**, 234505 (2005).

[34] N. G. Hadjiconstantinou, A. L. Garcia, M. Z. Bazant, and G. He, Statistical error in particle simulations of hydrodynamic phenomena, J. Comput. Phys. **187**, 274 (2003).

[35] T. A. Ho, D. V. Papavassiliou, L. L. Lee, and A. Striolo, Liquid water can slip on a hydrophilic surface, Proc. Natl. Acad. Sci. USA **108**, 16170 (2011).

[36] A. P. Bowles, C. D. F. Honig, and W. A. Ducker, No-slip boundary condition for weak solid-liquid interactions, J. Phys. Chem. C **115**, 8613 (2011).

[37] G. J. Wang and N. G. Hadjiconstantinou, Universal molecular-kinetic scaling relation for slip of a simple fluid at a solid boundary, Phys. Rev. Fluids **4**, 064201 (2019).

[38] H. Matsubara, M. Murase, Y. H. Mori, and A. Nagashima, Measurement of the surface tensions and the interfacial tensions of n-pentane-water and R 113-water systems, Int. J. Thermophys. **9**, 409 (1988).

[39] P. Petrov and I. Petrov, A combined molecular-hydrodynamic approach to wetting kinetics, Langmuir **8**, 1762 (1992).

[40] N. G. Hadjiconstantinou and A. T. Patera, A variationally consistent finite element approach to the two-fluid internal contact-line problem, Int. J. Numer. Methods Fluids **34**, 711 (2000).